



High-purity orbital angular momentum states from a visible metasurface laser

Hend Sroor¹, Yao-Wei Huang^{2,3}, Bereneice Sephton¹, Darryl Naidoo^{1,4}, Adam Vallés^{1,8}, Vincent Ginis^{2,5}, Cheng-Wei Qiu³, Antonio Ambrosio^{6,7}, Federico Capasso^{1,2} and Andrew Forbes¹✉

Orbital angular momentum (OAM) from lasers holds promise for compact, at-source solutions for applications ranging from imaging to communications. However, conjugate symmetry between circular spin and opposite helicity OAM states ($\pm\ell$) from conventional spin-orbit approaches has meant that complete control of light's angular momentum from lasers has remained elusive. Here, we report a metasurface-enhanced laser that overcomes this limitation. We demonstrate new high-purity OAM states with quantum numbers reaching $\ell=100$ and non-symmetric vector vortex beams that lase simultaneously on independent OAM states as much as $\Delta\ell=90$ apart, an extreme violation of previous symmetric spin-orbit lasing devices. Our laser conveniently outputs in the visible, producing new OAM states of light as well as all previously reported OAM modes from lasers, offering a compact and power-scalable source that harnesses intracavity structured matter for the creation of arbitrary chiral states of structured light.

In recent years it has become possible to tailor light in what is commonly referred to as structured light¹, supporting applications including high-bandwidth optical communication^{2–5}, access to high-dimensional quantum states^{6,7}, enhanced resolution in imaging⁸ and microscopy⁹ and control of matter by optical trapping and tweezing^{10,11}. Foremost among the family of structured light fields are those related to chiral light, which carries spin angular momentum and orbital angular momentum (OAM)¹², the latter characterized by a helical phase $\exp(i\ell\phi)$ about the azimuth (ϕ) with helicity ℓ . Driven by the many applications these beams have spurred¹³, much attention has been focused on their efficient creation.

Scalar OAM modes are easily created by dynamic phase approaches¹⁴, while geometric phase is a convenient mechanism for creating vector combinations of spin and OAM^{15–21}, forming cylindrical vector vortex beams that are rotationally symmetric complex states of light with an internal intensity null due to a polarization singularity²². They are conveniently expressed on the higher-order Poincaré sphere (HOPS)^{23,24}, where the poles are combinations of left- and right-circular spin angular momentum states ($\pm\sigma$) combined with symmetrical left- and right-helicity OAM states ($\pm\ell$). This vector addition has opened many exciting possibilities for new applications that exploit chiral control of both spin angular momentum and OAM degrees of freedom of light^{25–27}.

An ongoing challenge is to control light's chirality, spin and orbital at source^{28–31}. So far, advances have been limited, in part due to fundamental symmetry restrictions when using geometric phase and topological photonics and in part due to implementation restrictions, for example, in regard to the physical size and spatial resolution of the optical elements. Such advances include the generation of symmetric OAM states via the geometric phase^{32,33}, as integrated on-chip devices^{34–40}, in organic lasers⁴¹ and as fibre lasers⁴². Despite these impressive advances, breaking the symmetry of the spin and orbital states for arbitrary angular momentum control of light

at source has remained elusive. Arbitrary angular momentum control requires the ability to produce any desired spin-orbital chiral state of light, including arbitrary, differing and non-symmetric OAM values coupled to user-defined polarizations, an infinitely larger set than the special case of symmetric OAM states, allowing access to super-chiral light with high angular momentum. In contrast, OAM lasers so far have been demonstrated with only symmetric superpositions of $\pm\ell$ and $\pm\sigma$, which add to a total angular momentum of zero, and with modest OAM values of up to $|\ell|=\pm 10$ (ref. 32). However, super-chiral light with high angular momentum is known to be important in many fundamental and applied studies, for example, in quantum studies with Bose-Einstein condensates, remote sensing with structured light, accurate rotation measurements, metrology of chiral media and for larger photon information capacity⁴³.

Here, we report a laser with an intracavity metasurface for control of light's angular momentum at source. We design custom metasurfaces for arbitrary OAM coupling to linear polarization states, including a metasurface with an extreme imbedded helicity of up to $\ell=100$. By doing so, we are able to produce new chiral states of light from a laser, including simultaneous lasing across vastly differing and non-symmetric OAM values that are up to $\Delta\ell=90$ apart, an extreme violation of previous symmetric spin-orbit (SO) lasing devices, and demonstrate some intriguing lasing phenomena, for example, vortex splitting inside a laser medium and coherent lasing across modes with no spatial overlap. By designing a cavity for mode metamorphosis, our laser is able to generate ultrahigh-purity OAM modes with orders of magnitude enhanced purity over their externally created counterparts, which we show with OAM modes up to $\ell=100$. Importantly, the coupling to linear polarization states facilitates a compact design with a reduction in complexity and number of optical elements over previous geometric phase lasers, the latter of course restricted to only symmetric states. In addition to these

¹School of Physics, University of the Witwatersrand, Wits, South Africa. ²Harvard John A. Paulson School of Engineering and Applied Sciences, Harvard University, Cambridge, MA, USA. ³Department of Electrical and Computer Engineering, National University of Singapore, Singapore, Singapore. ⁴CSIR National Laser Centre, Pretoria, South Africa. ⁵Applied Physics, Vrije Universiteit Brussel, Brussels, Belgium. ⁶Center for Nanoscale Systems, Harvard University, Cambridge, MA, USA. ⁷CNST - Fondazione Istituto Italiano di Tecnologia Via Giovanni Pascoli, Milan, Italy. ⁸Present address: Molecular Chirality Research Center, Chiba University, Inage-ku, Chiba, Japan. ✉e-mail: andrew.forbes@wits.ac.za

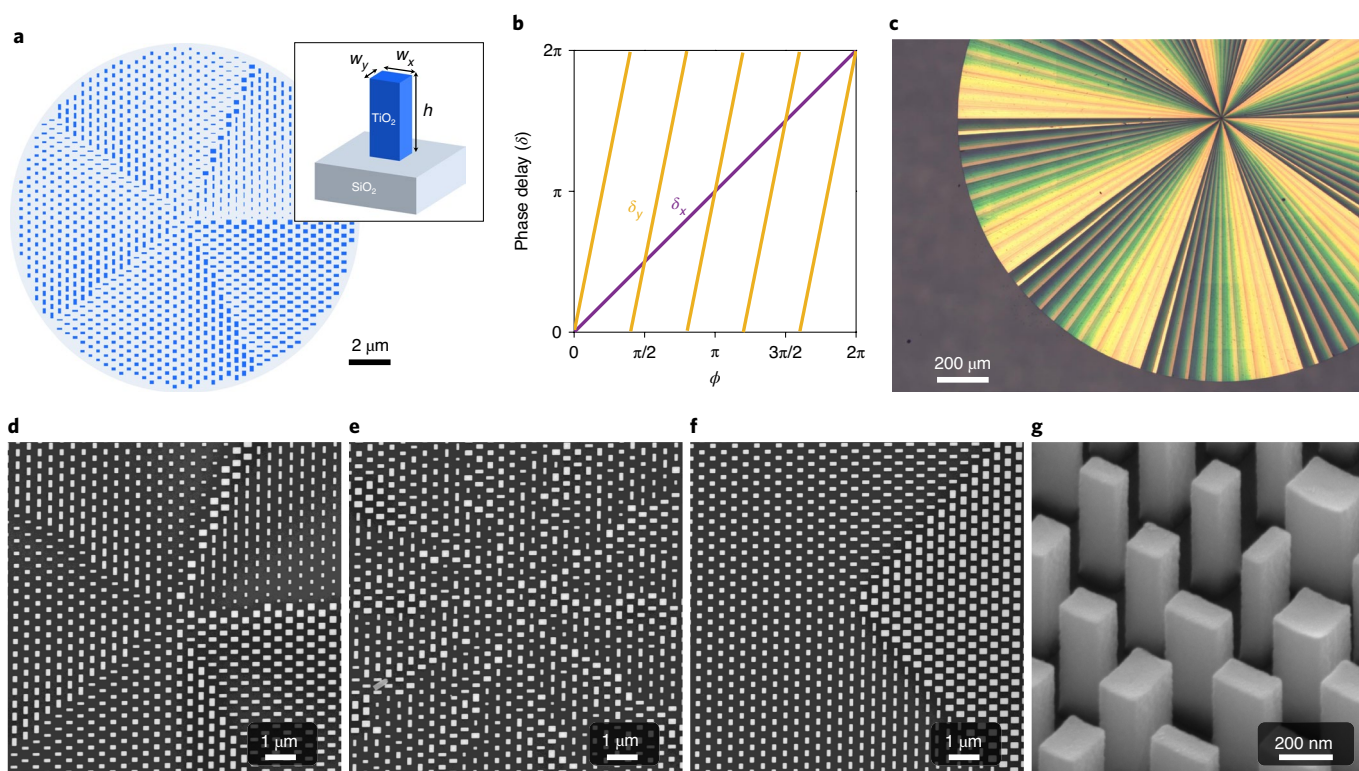


Fig. 1 | Metasurface design and characterization. **a**, Schematic of the central part of our metasurface, which imprints two kinds of helical phase profiles for x - and y -incident polarization, resulting in output beams with OAM of $\ell_1 h$ and $\ell_2 h$. The metasurface elements are rectangular nanopillars made of amorphous TiO_2 with fixed height, $h = 600$ nm. By changing the width along the x and y directions, the nanoposts impart azimuthal phase delays given by δ_x and δ_y . **b**, Required phase delays for output beam OAM values of $\ell_1 = 1$ and $\ell_2 = 5$ (JP2). **c**, Optical micrograph of JP3 with OAM values of $\ell_1 = 10$ and $\ell_2 = 100$. **d–f**, Scanning electron micrographs of the central parts of JP1 (**d**), JP2 (**e**) and JP3 (**f**). **g**, Tilted scanning electron micrograph showing the nanoposts of JP2. All our J-plates were fabricated using the process detailed in ref. 45.

advances, our laser conveniently operates in the visible, produces all previous observed OAM states from lasers, while our metasurface fabrication facilitates high damage threshold operation.

Results

Metasurface J-plates. In this work we design and fabricate metasurfaces to engineer a compact visible metasurface laser for general states of super-chiral light. Our SO device, which we call a J-plate, is a dielectric metasurface made of amorphous TiO_2 nanoposts (with rectangular section) on a fused-silica substrate (Fig. 1a). Each post has a height of 600 nm, while the width and length (W_x , W_y) change so as to impart a different phase delay to the propagating visible light at a wavelength of 532 nm. More specifically, the J-plate can impart different azimuthal phase delays δ_x and δ_y on the field polarization components (horizontal and vertical) (Fig. 1b).

In the past, devices based on both liquid crystals and metasurfaces have been proposed that use the Pancharatnam–Berry (PB) phase to impart OAM to circularly polarized beams. In this case, all the elements of the device, either liquid-crystal molecules or nanoposts, are the same but azimuthally oriented to impose a helical wavefront to the propagating light. In such devices, the $\pm h$ spin momentum of the incident light is converted into the opposite spin (opposite polarization handedness) and $\pm \ell h$ of OAM (while an opposite angular momentum is transferred to the device itself). The angular momentum of each component therefore cancels for zero net angular momentum. Lasers based on this concept have been demonstrated using liquid crystals with up to $\ell = \pm 10$ (ref. 32) and metasurfaces up to $\ell = \pm 3$ (ref. 33), and similar concepts have been exploited for on-chip control of scalar OAM up to $\ell = \pm 2$ (ref. 36).

Table 1 | Three metasurface designs (JP1, JP2 and JP3) for arbitrary angular momentum control from our laser

Incident state	$ H, \ell = 0\rangle$	$ V, \ell = 0\rangle$
JP1	$ H, \ell = -1\rangle$	$ V, \ell = 1\rangle$
JP2	$ H, \ell = 1\rangle$	$ V, \ell = 5\rangle$
JP3	$ H, \ell = 10\rangle$	$ V, \ell = 100\rangle$

The incident scalar Gaussian states are converted into arbitrary vector OAM states.

Our metasurface is more general than these devices and is designed to convert any two orthogonal polarization states of the incident light into helical modes with any arbitrary value of OAM, ℓ_1 and ℓ_2 , and not just opposite values. This is possible by controlling the PB phase, the overall phase and the form birefringence of each element^{44,45}. We designed and fabricated three such elements, JP1, JP2 and JP3, with the SO coupling described in Table 1. JP1 allows us to replicate previous SO lasers that produce only symmetric states, that is, $\ell_1 = -\ell_2$ (the linear polarization can be flipped with a quarter-waveplate to produce cylindrical vector vortex beams; see Supplementary Information) while JP2 and JP3 allow for the most general OAM states to be produced from a laser.

Figure 1c presents an optical microscope image of JP3, which produces helical modes with OAM of $\ell = 10$ and $\ell = 100$ for horizontally and vertically polarized incident light, respectively. The implemented azimuthal phase gradient is visible in the optical image of the device as a colour variation (nanoposts with different

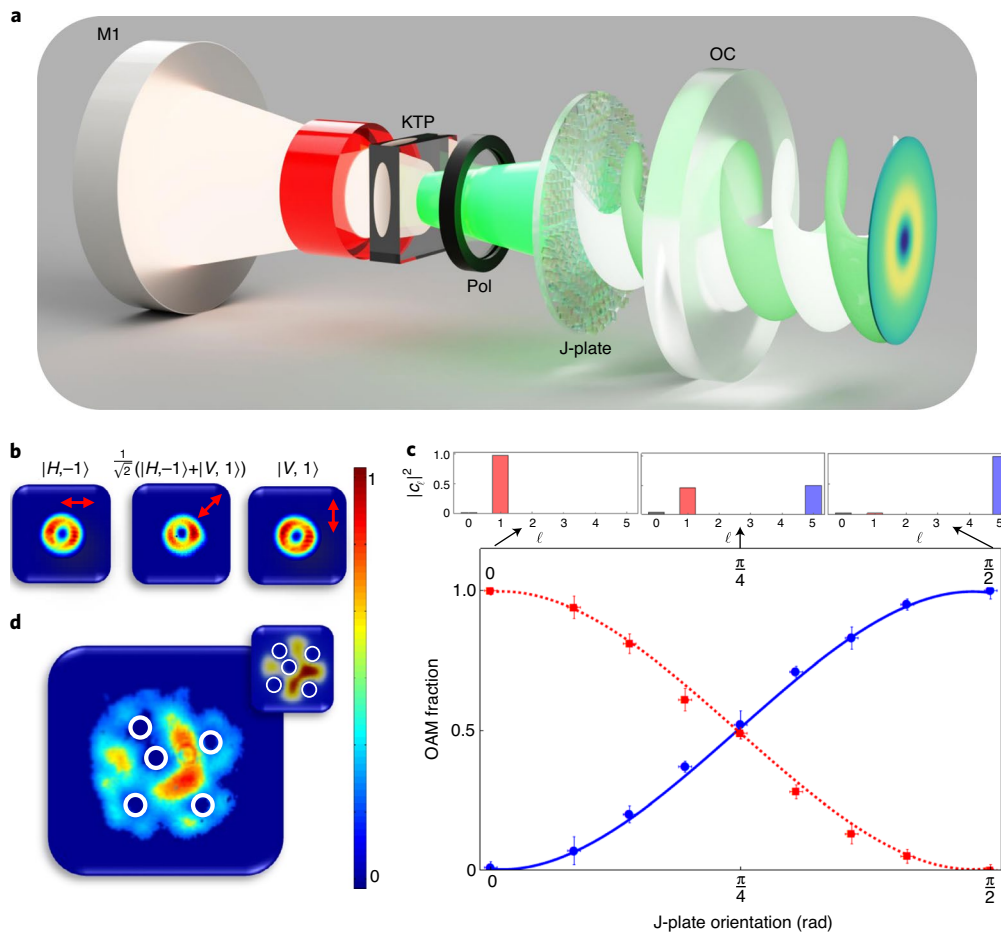


Fig. 2 | Metasurface laser and modes. **a**, Illustration of laser cavity with an intracavity nonlinear crystal (KTP), polarizer (Pol) and metasurface (J-plate), excited by an infrared pump (between mirror M1 and the back KTP crystal face), with the green light emerging from the output coupler (OC) mirror. **b**, Replication of previous SO laser results showing symmetric states of $|\ell| = \pm 1$ for three orientations of the fast axis of JP1 (red arrows). **c**, Creation of a new angular momentum state with $\ell_1 = 1$ and $\ell_2 = 5$. As θ (J-plate orientation) is varied, the modal spectrum shifts from $|H, 1\rangle$ (red squares) to $|V, 5\rangle$ (blue circles), in agreement with theory (curves). Insets: the OAM spectrum at different θ . Error bars show standard deviations. **d**, Creation of an arbitrary vector superposition state of coherently mixed vortices showing five distinct phase singularities (indicated by white circles), in agreement with theory (shown in the inset). All results were taken at an average pump energy of 230 mJ. For **b** and **d**, the colour bar shows normalized intensity plotted with a false colour scale of 0 to 1.

shapes have different scattering resonance frequencies, resulting in a colourful optical image). Note that it is easy to distinguish 10 sectors, each made of 10 inner sectors. This means that, for the helical mode resulting from incident vertically polarized light, to generate a beam with OAM $\ell = 100$, a 2π azimuthal phase variation must be accumulated in an angle of just $2\pi/100$. Such a high phase gradient has never been implemented into any metasurface before. Figure 1d–f presents scanning electron microscopy (SEM) images of the metasurface devices summarized in Table 1 (from left to right: JP1, JP2 and JP3, respectively): the nanoposts have different shapes and orientations to implement the necessary phase gradient by combining the propagation phase, PB phase and form birefringence as described earlier. This is visualized in Fig. 1g, which shows a tilted SEM image of a few typical nanoposts constituting one of our devices.

Intracavity implementation. Our laser, shown schematically in Fig. 2a, was constructed as a frequency-doubled cavity that converts the infrared fundamental frequency of Nd:YAG ($\lambda = 1,064$ nm) to the second-harmonic green ($\lambda = 532$ nm) through an intracavity nonlinear crystal (KTP). The J-plate was placed in the resonant green cavity to provide a geometry that represents the first visible

metasurface-assisted laser. We will refer to this geometry as our ‘metasurface laser’.

The concept of the laser design exploits a unique feature of our metasurfaces, namely OAM coupling to linear polarization states. The resonant mode morphs from a linearly polarized Gaussian-like enveloped beam at one end of the cavity to an arbitrary angular momentum state at the other. Although a polarizer was required for selection of the horizontal polarization state before the J-plate, the polarization of the light traversing the J-plate was controlled by simply rotating the J-plate itself. This relative rotation can be viewed as the alignment of the polarization state to the optical fast axis of the J-plate.

The intracavity light undergoes multiple passes backwards and forwards through the metasurface (see Supplementary Information and Supplementary Video 1). Starting as $|H, 0\rangle$ (horizontally polarized and no OAM), it is converted to the desired combination within the laser, say $\cos\theta|H, \ell_1\rangle + \sin\theta|V, \ell_2\rangle$ (where θ is the angle of the fast axis of the J-plate with respect to the horizontal), the most general OAM state possible and a state never previously created from a laser cavity. As the SO effect couples OAM to linear polarization states, mirror reflections do not result in any spin flipping, and only the OAM handedness changes sign; conventional

SO coupling lasers flip both the spin and OAM, which prohibits a simple two-mirror cavity (see Supplementary Information). The present design thus leads to a reduction in the number of optical elements and the cavity complexity compared with previous designs. On reflection from the output coupler mirror back to the J-plate, the state is $\cos\theta|H, -\ell_1\rangle + \sin\theta|V, -\ell_2\rangle$. From the reciprocity of the metasurface, the initial state $|H, 0\rangle$ is regained, which then returns through the polarizer to the KTP crystal. Ordinarily, vastly differing ℓ modes would occupy different crystal gain regions and therefore would lase independently; in our design, the modes overlap within the crystal, ensuring spatial coherence even without any spatial overlap at the output. The state $\cos\theta|H, \ell_1\rangle + \sin\theta|V, \ell_2\rangle$ is then a repeating mode after each round trip and thus full angular momentum control from the laser is possible.

Generation of symmetric OAM and HOPS states. We first replicate previous geometric phase lasers by creating linear HOPS beams with conjugate OAM states, that is $|\ell_1| = -|\ell_2|$. Figure 2b presents example output modes at different angles (shown as inset red arrows) of the JP1 metasurface. As expected, the output modes are annular-shaped intensity profiles that remain invariant during rotation of the metasurface (all states on the HOPS have the same intensity profile) while modal analysis confirmed the expected OAM structure (see Supplementary Information).

Arbitrary angular momentum control. To demonstrate arbitrary angular momentum control we used JP2 to create laser modes with asymmetric OAM states described by $\cos\theta|H, 1\rangle + \sin\theta|V, 5\rangle$. As JP2 is rotated, the output mode shifts in weighting from an OAM of $\ell_1 = 1$ to an OAM of $\ell_2 = 5$, with arbitrary vector superpositions in between (shown in Fig. 2c, with insets showing the measured OAM spectrum at the different rotation angles). At intermediate JP2 rotations a superposition of the two OAM modes is present, including the special case of an equal OAM fraction. When added coherently, the prediction is a non-trivial superposition of vortices with a central vortex of charge ℓ_1 surrounded by $|\ell_1 - \ell_2|$ single-charged peripheral vortices of sign $\ell_2/|\ell_2|$ (ref. 46). In our case, this translates to a central vortex of charge +1 with four surrounding vortices of charge +1 (the sum does not add to 6, contrary to what one might have expected). This was observed experimentally and is shown in Fig. 2d (the inset shows the theoretical prediction). The singularities are highlighted by white circles. This demonstrates that our laser can not only reproduce all previous SO results with a simpler cavity configuration, but is also able to produce more exotic states of light.

Having demonstrated arbitrary angular momentum control within a laser, we now demonstrate extreme SO asymmetric coupling using JP3 in a metasurface laser for an output state of $\cos\theta|H, 10\rangle + \sin\theta|V, 100\rangle$. Here, the difference in helicity is $\Delta\ell = |\ell_1 - \ell_2| = 90$. The successful generation of this general OAM state is shown in Fig. 3. As the weighting of the states is altered through JP3 rotation (control of θ), the superposition state changes from $|H, 10\rangle$ on one pole to $|V, 100\rangle$ on the other. Intermediate states show the progression from lasing on one mode to the other: contrary to the previous asymmetric case ($\ell_1 = 1$ and $\ell_2 = 5$), here the composite-vortex beams are found to possess a structure that contains two superimposed concentric rings. This can be understood as $\ell_1 \ll \ell_2$, and thus each state is simultaneously lasing but occupying completely different spatial regions after the metasurface (but overlapping in the crystal for coherence).

Modal purity. In Fig. 4 we compare the purity of the OAM laser modes (blue) to the corresponding externally generated modes with the same J-plate (red) for $\ell = 10$ and $\ell = 100$ using modal decomposition, allowing the modal power contribution to each mode in the Laguerre–Gaussian (LG) basis to be measured and calculated (see Supplementary Information). The LG basis has both azimuthal (ℓ)

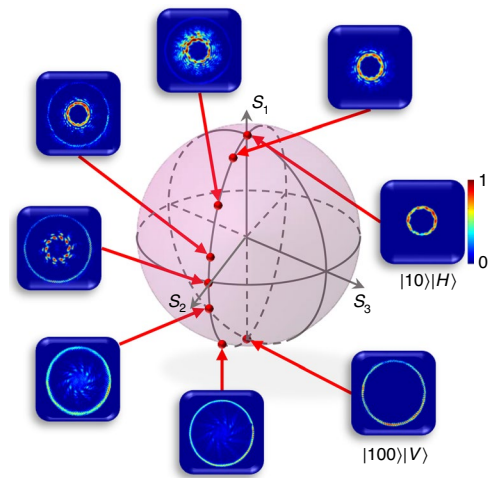


Fig. 3 | Extreme SO lasing. Various measured states from the laser, displayed on a generalized OAM sphere. Here, the poles are asymmetric with OAM order $\ell_1 = 10$ (north pole) and $\ell_2 = 100$ (south pole). The transition from one to the other allows visualization of lasing across vastly differing OAM values as superpositions with two concentric rings. The operating pump energy was 315 mJ. The colour bar shows normalized intensity plotted with a false colour scale of 0 to 1.

and radial (p) terms, the former responsible for the OAM content. Ideally, a pure OAM mode would have high power content in the desired ℓ and $p = 0$ mode. Figure 4a reports the results for $\ell = 10$ modes: we see that generation of the modes from inside the laser cavity yields a high OAM purity of 92% (compared to only 72% for external generation using the same metasurface). More telling is the fact that the 92% is contained entirely in the desired $p = 0$ mode, whereas the 72% for external generation is spread across numerous radial modes. The bottom panel of Fig. 4a shows a more detailed view, with the measured and calculated radial mode expansion, confirming that the laser produces ultrahigh-purity OAM modes in comparison to externally generated modes (the interesting damped oscillatory nature of the p -mode weightings is predicted by theory; see Supplementary Information). This is echoed in the beam structures shown in Fig. 4b,c for the internally and externally generated modes, respectively, with the former showing the telltale signs of a radial ring structure rather than the single ring of the desired vortex state.

This external purity degradation becomes more pronounced at higher OAM values⁴⁷. In Fig. 4d,e we show the $\ell = 100$ externally generated mode and the laser mode, respectively. The visual effect is striking: distinct spatial ring structures and a radial outward spread in intensity can be observed in the externally generated mode, compared to the well-defined annular ring structure for the laser generated mode. For the $\ell = 100$ mode shown in Fig. 4d, the experimentally measured 71% OAM purity has only ~13% (Supplementary Table I) in the desired $\ell = 100$, $p = 0$ mode, while the laser mode shown in Fig. 4e has a purity of ~90% in the $p = 0$ mode. This is shown quantitatively in Fig. 4f, with the OAM mode spectrum shown for the laser mode (blue bars) and the externally created mode (red lollipop). There is a slight decrease in purity relative to the $\ell = 10$ mode, but the purity remains very high.

In our comparative analysis, all decompositions of the laser generated modes were performed at a common scale of w_0 (the embedded Gaussian radius), while the scale for the external modes was optimally adjusted for each mode to $w_{\text{opt}} = w_0 / \sqrt{|\ell| + 1}$, an optimal scale to maximize the power content of the $p = 0$ mode. Figure 4g shows a comparison of the laser mode purity measured at the scale w_0 versus the external generated beams measured at the

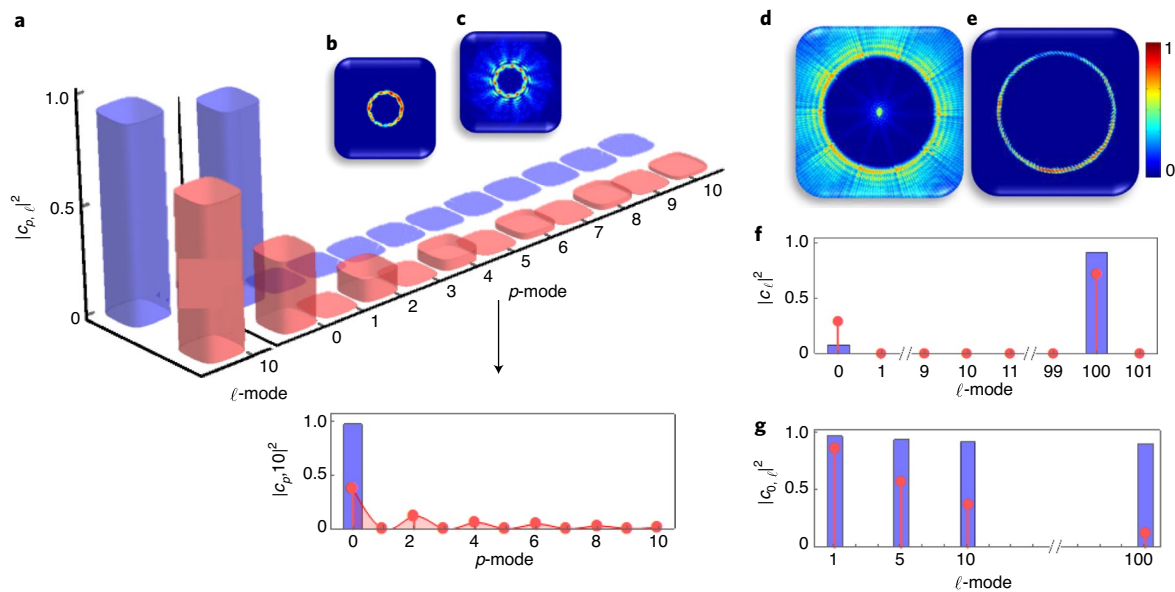


Fig. 4 | Ultrapure OAM lasing modes. **a**, Measured modal spectrum for $\ell=10$, both internal (blue) and external (red) to the laser. $|c_{p,\ell}|^2$ is the modal power in the p th radial mode and ℓ th OAM mode. **b,c**, The corresponding beam intensities are shown for the internal modes (**b**) and external modes (**c**). The bottom inset in **a** shows an enlarged version with experimental data (lollipop bars) and theoretical predictions (solid line). **d,e**, The same analysis, performed on the $\ell=100$ modes, showing intensity profiles created external (**d**) and internal (**e**) to the laser. The colour bar shows normalized intensity plotted with a false colour scale of 0 to 1. **f**, OAM distribution of external (red lollipops) and laser (blue bars) modes, where $|c_{\ell}|^2$ represents the total OAM modal power (summed over all p modes). **g**, Comparison of the $p=0$ mode weightings for the externally generated beams (red lollipops) versus cavity modes (blue bars). The operating pump energy was 315 mJ for all measurements.

scale w_{opt} for all modes generated in this study (see Supplementary Table I for full measurement values). Although the scale for the external beam decomposition changes drastically across the ℓ spectrum, our laser produces much higher purity for all ℓ at the same intuitive scale, w_0 .

There are several mechanisms that give rise to this enhanced purity. Recall that, external to the laser, the radial modes appear because of a missing amplitude term; in the laser the lowest loss mode has the required amplitude by cavity diffraction, while the radial modes that are created are suppressed. For example, diffraction results in a resonant mode that has a Gaussian-like envelope (but is not Gaussian) at the KTP crystal for all OAM modes, while the output OAM scale is fixed by the radius of curvature of the output mirror and the cavity length. The resonant mode inside the cavity differs from plane to plane: at the plane of the J-plate it has the required (missing) amplitude term to produce a high-purity LG $p=0$ at the output coupler. Furthermore, the multiple passes in the green cavity ensure radial mode suppression by gain-assisted filtering, by virtue of the overlap of the resonant mode and the infrared pump mode. The radial modes are similarly suppressed by the mode-dependent resonant frequencies of the cavity, enhanced further by the limited excitation of radial modes through nonlinear modal coupling inside the crystal⁴⁸. Together then, the cavity suppresses radial modes by a combination of diffraction-induced filtering, resonance-induced filtering and gain-assisted filtering. All these mechanisms prevail to allow high-purity OAM lasing.

Discussion and conclusion

The concept of the laser exploits our metasurface's extraordinary feature of coupling arbitrary OAM to arbitrary spin states, which we have demonstrated with OAM up to $\ell=100$ and with a large OAM differential between modes of up to $\Delta\ell=90$, representing intracavity SO symmetry-breaking for super-chiral light. The metasurface approach has the additional benefits of a high damage

threshold⁴⁹ and spatial resolution down to the nanometre scale for a well-defined singularity with low loss. Our approach has allowed the demonstration of an order-of-magnitude higher OAM than previously reported from geometric phase lasers, a high total angular momentum in our vector states (symmetric lasers have zero total angular momentum), all in ultrahigh-purity modes in the visible.

What we find particularly exciting is that our approach lends itself to many laser architectures. For example, one could increase the gain volume and metasurface size to produce a bulk laser for high power or one could shrink the system down to a microchip using a monolithic metasurface design. Although we have controlled the intracavity polarization and rotated the J-plate for mode control, the lasing mode could be controlled by manipulating the polarization of the pump beam with a judiciously chosen nonlinear crystal⁵⁰ for a dynamically switchable laser output. Thus, our work represents an important step towards merging the research in bulk OAM lasers and that of on-chip devices.

In summary, we have demonstrated a laser that produces all OAM states previously observed from lasers as well as new forms of chiral light not observed from lasers until now. The demonstrated performance, versatility in design and power-handling capabilities of our approach point to an exciting route to control light's angular momentum at the source.

Online content

Any methods, additional references, Nature Research reporting summaries, source data, extended data, supplementary information, acknowledgements, peer review information; details of author contributions and competing interests; and statements of data and code availability are available at <https://doi.org/10.1038/s41566-020-0623-z>.

Received: 25 April 2019; Accepted: 18 March 2020;
Published online: 27 April 2020

References

- Rubinsztein-Dunlop, H. et al. Roadmap on structured light. *J. Opt.* **19**, 013001 (2016).
- Willner, A. E. et al. Optical communications using orbital angular momentum beams. *Adv. Opt. Photon.* **7**, 66–106 (2015).
- Wang, J. Advances in communications using optical vortices. *Photon. Res.* **4**, B14–B28 (2016).
- Wang, J. Data information transfer using complex optical fields: a review and perspective. *Chin. Opt. Lett.* **15**, 030005 (2017).
- Ndagano, B., Nape, I., Cox, M. A., Rosales-Guzman, C. & Forbes, A. Creation and detection of vector vortex modes for classical and quantum communication. *J. Lightw. Technol.* **36**, 292–301 (2018).
- Krenn, M., Malik, M., Erhard, M. & Zeilinger, A. Orbital angular momentum of photons and the entanglement of Laguerre–Gaussian modes. *Philos. Trans. R. Soc. A* **375**, 20150442 (2017).
- Erhard, M., Fickler, R., Krenn, M. & Zeilinger, A. Twisted photons: new quantum perspectives in high dimensions. *Light Sci. Appl.* **7**, 17111–17146 (2018).
- Moreau, P. A., Toninelli, E., Gregory, T. & Padgett, M. J. Ghost imaging using optical correlations. *Laser Photon. Rev.* **12**, 1700143 (2018).
- Maurer, C., Jesacher, A., Bernet, S. & Ritsch-Marte, M. What spatial light modulators can do for optical microscopy. *Laser Photon. Rev.* **5**, 81–101 (2011).
- Grier, D. G. A revolution in optical manipulation. *Nature* **424**, 810–816 (2003).
- Padgett, M. J. & Bowman, R. Tweezers with a twist. *Nat. Photon.* **5**, 343–348 (2011).
- Allen, L., Beijersbergen, M. W., Spreeuw, R. J. C. & Woerdman, J. P. Orbital angular momentum of light and the transformation of Laguerre–Gaussian laser modes. *Phys. Rev. A* **45**, 8185–8189 (1992).
- Padgett, M. J. Orbital angular momentum 25 years on. *Opt. Express* **25**, 11265–11274 (2017).
- Heckenberg, N., McDuff, R., Smith, C. & White, A. Generation of optical phase singularities by computer-generated holograms. *Opt. Lett.* **17**, 221–223 (1992).
- Marrucci, L., Manzo, C. & Paparo, D. Optical spin-to-orbital angular momentum conversion in inhomogeneous anisotropic media. *Phys. Rev. Lett.* **96**, 163905 (2006).
- Brasselet, E., Murazawa, N., Misawa, H. & Juodkazis, S. Optical vortices from liquid crystal droplets. *Phys. Rev. Lett.* **103**, 103903 (2009).
- Brasselet, E. Tunable high-resolution macroscopic self-engineered geometric phase optical elements. *Phys. Rev. Lett.* **121**, 033901 (2018).
- Nassiri, M. G. & Brasselet, E. Multispectral management of the photon orbital angular momentum. *Phys. Rev. Lett.* **121**, 213901 (2018).
- Nersisyan, S. R., Tabiryan, N. V., Steeves, D. M. & Kimball, B. R. The promise of diffractive waveplates. *Opt. Photon. News* **21**, 40–45 (2010).
- Rubano, A., Cardano, F., Piccirillo, B. & Marrucci, L. Q-plate technology: a progress review. *J. Opt. Soc. Am. B* **36**, D70–D87 (2019).
- Piccirillo, B., Slussarenko, S., Marrucci, L. & Santamato, E. The orbital angular momentum of light: genesis and evolution of the concept and of the associated photonic technology. *Riv. Nuovo Cimento* **36**, 501–555 (2013).
- Zhan, Q. Cylindrical vector beams: from mathematical concepts to applications. *Adv. Opt. Photon.* **1**, 1–57 (2009).
- Milione, G., Sztul, H., Nolan, D. & Alfano, R. Higher-order Poincaré sphere, Stokes parameters, and the angular momentum of light. *Phys. Rev. Lett.* **107**, 053601 (2011).
- Holleccek, A., Aiello, A., Gabriel, C., Marquardt, C. & Leuchs, G. Classical and quantum properties of cylindrically polarized states of light. *Opt. Express* **19**, 9714–9736 (2011).
- Rosales-Guzmán, C., Ndagano, B. & Forbes, A. A review of complex vector light fields and their applications. *J. Opt.* **20**, 123001 (2018).
- Cardano, F. & Marrucci, L. Spin-orbit photonics. *Nat. Photon.* **9**, 776–778 (2015).
- Otte, E., Alpmann, C. & Denz, C. Polarization singularity explosions in tailored light fields. *Laser Photon. Rev.* **12**, 1700200 (2018).
- Forbes, A. Controlling light's helicity at the source: orbital angular momentum states from lasers. *Philos. Trans. R. Soc. A* **375**, 20150436 (2017).
- Omatsu, T., Miyamoto, K. & Lee, A. J. Wavelength-versatile optical vortex lasers. *J. Opt.* **19**, 123002 (2017).
- Wang, X. et al. Recent advances on optical vortex generation. *Nanophotonics* **7**, 1533–1556 (2018).
- Forbes, A. Structured light from lasers. *Laser Photon. Rev.* **13**, 1900140 (2019).
- Naidoo, D. et al. Controlled generation of higher-order Poincaré sphere beams from a laser. *Nat. Photon.* **10**, 327–332 (2016).
- Maguid, E. et al. Topologically controlled intracavity laser modes based on Pancharatnam–Berry phase. *ACS Photonics* **5**, 1817–1821 (2018).
- Cai, X. et al. Integrated compact optical vortex beam emitters. *Science* **338**, 363–366 (2012).
- Miao, P. et al. Orbital angular momentum microlaser. *Science* **353**, 464–467 (2016).
- Zambon, N. C. et al. Optically controlling the emission chirality of microlasers. *Nat. Photon.* **13**, 283–288 (2019).
- Li, H. et al. Orbital angular momentum vertical-cavity surface-emitting lasers. *Optica* **2**, 547–552 (2015).
- Xie, Z. et al. Ultra-broadband on-chip twisted light emitter for optical communications. *Light Sci. Appl.* **7**, 18001 (2018).
- Hayenga, W. E. et al. Direct generation of tunable orbital angular momentum beams in microring lasers with broadband exceptional points. *ACS Photonics* **6**, 1895–1901 (2019).
- Seghilani, M. S. et al. Vortex laser based on III–V semiconductor metasurface: direct generation of coherent Laguerre–Gauss modes carrying controlled orbital angular momentum. *Sci. Rep.* **6**, 38156 (2016).
- Stellinga, D. et al. An organic vortex laser. *ACS Nano* **12**, 2389–2394 (2018).
- Mao, D. et al. Ultrafast all-fiber based cylindrical-vector beam laser. *Appl. Phys. Lett.* **110**, 021107 (2017).
- Yao, A. M. & Padgett, M. J. Orbital angular momentum: origins, behavior and applications. *Adv. Opt. Photon.* **3**, 161–204 (2011).
- Devlin, R. C., Ambrosio, A., Rubin, N. A., Mueller, J. B. & Capasso, F. Arbitrary spin-to-orbital angular momentum conversion of light. *Science* **358**, 896–901 (2017).
- Devlin, R. C. et al. Spin-to-orbital angular momentum conversion in dielectric metasurfaces. *Opt. Express* **25**, 377–393 (2017).
- Baumann, S., Kalb, D., MacMillan, L. & Galvez, E. Propagation dynamics of optical vortices due to Gouy phase. *Opt. Express* **17**, 9818–9827 (2009).
- Sephton, B., Dudley, A. & Forbes, A. Revealing the radial modes in vortex beams. *Appl. Opt.* **55**, 7830–7835 (2016).
- Schwob, C. et al. Transverse effects and mode couplings in OPOS. *Appl. Phys. B* **66**, 685–699 (1998).
- Yao, J. et al. Investigation of damage threshold to TiO₂ coatings at different laser wavelength and pulse duration. *Thin Solid Films* **516**, 1237–1241 (2008).
- Taira, T., Sasaki, T. & Kobayashi, T. Polarization control of Q-switch solid-state lasers with intracavity SHG crystals. *Electron. Commun. Jpn* **2** **75**, 1–12 (1992).

Publisher's note Springer Nature remains neutral with regard to jurisdictional claims in published maps and institutional affiliations.

© The Author(s), under exclusive licence to Springer Nature Limited 2020

Methods

Our metasurface laser comprised a nonlinear crystal inside its own cavity, which itself was placed inside an infrared cavity, to achieve a resonant optical parametric oscillator configuration. The infrared gain medium was a 1.1% doped Nd:YAG crystal rod with dimensions of 76 mm (length) by 6.35 mm (diameter). The crystal was flash-lamp side-pumped. For second-harmonic generation, a nonlinear KTP crystal (type 0, $3 \times 3 \times 5$ mm³) was used to convert the intracavity infrared light ($\lambda = 1,064$ nm) of the Nd:YAG to second-harmonic green light at $\lambda = 532$ nm. The input face of the KTP crystal was antireflection-coated for $\lambda = 1,064$ nm and high-reflection-coated for $\lambda = 532$ nm, while the output face was highly transmissive at the second-harmonic wavelength ($\lambda = 532$ nm) and was high-reflection-coated at $\lambda = 1,064$ nm. The back reflector mirror M1 was a concave mirror with radius of curvature (ROC) of 400 mm and had a reflectivity of 98%, whereas the output coupler mirror (ROC = 200 mm) was highly reflective at $\lambda = 1,064$ nm while coupling 0.8% of the intracavity green light outside the cavity. The KTP crystal was placed at the infrared beam waist position while the J-plate was placed adjacent to the output coupler mirror. Both theory and experiment have shown that the cavity length is far more critical than the position of the J-plate inside the cavity. This can be understood from the fact that the mode discrimination is dependent on the size of the resonant mode at the crystal and the resonant frequencies, both influenced by cavity length, whereas the position of the J-plate merely impacts the spectrum of modes created, finally to be removed by the cavity after many round trips by the discrimination process. The resonant mirrors were spaced by an effective distance of ~600 mm. The empty (with no J-plate) cavity length was adjusted so that the spot size of the $\lambda = 1,064$ nm beam at the crystal input surface was measured to be 81 μm (close to the calculated value of 82.3 μm), while the spot size of the output green beam was 62 μm (close to the calculated value of 64.4 μm) at the KTP crystal. This ensured that the green cavity would have excellent gain overlap for only low radial modes. The laser was gain-switched with the $\lambda = 1,064$ nm output pulse duration of 40 ns. The conversion efficiency of the KTP was 18% under the single-pass configuration and increased to ~61% once the output coupler mirror was in place to form the green resonant cavity. The isolation of the $\lambda = 532$ nm output from the cavity output coupler mirror was confirmed by measuring the emission spectra of the output (see Supplementary Information) using a spectrometer (Ocean Optics). We quantitatively confirmed the advantages of our intracavity approach versus an equivalent extracavity generation approach using the modal decomposition technique. The output beam was directed toward a spatial light modulator, which was digitally encoded with a match filter in the LG basis. The resultant field was transformed in the Fourier plane using a Fourier lens ($f = 300$ mm), which was positioned a focal length from the plane of the spatial light modulator. The on-axis

intensities at the Fourier plane after the lens were recorded using a charge-coupled device camera. After subtracting any noise from the system, the modal weightings were evaluated by normalizing the on-axis intensities.

Data availability

The data that support the plots within this paper and other findings of this study are available from the corresponding author upon reasonable request.

Code availability

The codes that support the plots and multimedia files within this paper are available from the corresponding author upon reasonable request.

Acknowledgements

A.V. acknowledges support from the Claude Leon Foundation. This work was performed, in part, at the Center for Nanoscale Systems (CNS), a member of the National Nanotechnology Coordinated Infrastructure (NNCI), which is supported by the NSF under award no. 1541959. CNS is a part of Harvard University. F.C. is supported by funding from the Air Force Office of Scientific Research (grant nos. MURI: FA9550-14-1-0389, FA9550-16-1-0156), and the King Abdullah University of Science and Technology (KAUST) Office of Sponsored Research (OSR) (award no. OSR-2016-CRG5-2995). Y.-W.H. and C.-W.Q. are supported by the National Research Foundation, Prime Minister's Office, Singapore under its Competitive Research Program (CRP award no. NRF-CRP15-2015-03).

Author contributions

H.S., D.N., B.S. and A.V. performed experiments with custom optics designed and fabricated by Y.-W.H. and A.A. All authors contributed to data analysis and writing of the manuscript. A.F., F.C. and C.-W.Q. supervised the project.

Competing interests

The authors declare no competing interests.

Additional information

Supplementary information is available for this paper at <https://doi.org/10.1038/s41566-020-0623-z>.

Correspondence and requests for materials should be addressed to A.F.

Reprints and permissions information is available at www.nature.com/reprints.